Local Flow Effects on Noise Prediction of Transonic Truss-Braced Wing Landing Gear

Jason C. June*, Alexandra M. Hickey †, and Yueping Guo ‡
NASA Langley Research Center, Hampton, VA 23681, USA

The local flow velocity is a primary scaling parameter to the strength of noise sources on landing gear. Airframe geometry, particularly the landing gear integration details can result in large, localized deviations from the freestream velocity. The transonic truss-braced wing aircraft concept presents a unique situation where the main landing gear is integrated into a wing strut rather than the traditional wing- or body-mounted gear. Existing parametric models of the velocity in the gear region are limited to conventional aircraft; application to unconventional configurations has the potential to introduce error into the noise prediction. Reynolds-averaged Navier-Stokes simulations of the flow around a transonic truss-braced wing at several flight conditions comprise a database to model the local flow velocity near the gear. A polynomial function dependent on the distance from the strut and angle of attack is sufficient to model the flow dependence. This model addresses a gap in accurate system noise prediction of this particular unconventional configuration, resulting in a 2.4 EPNdB difference in main gear noise relative to a previously-used model.

Nomenclature

A, B	=	coefficients
α	=	angle of attack
c	=	chord
c_∞	=	sound speed
c_l	=	sectional lift coefficient
c_p	=	coefficient of pressure
δx	=	wing-strut axial quarter-chord offset
δz	=	wing-strut vertical quarter-chord offset
Δx	=	axial sampling spacing
Δz	=	vertical sampling spacing
Γ	=	circulation
k	=	lifting line geometric function
μ	=	dynamic viscosity
M	=	Mach number
N	=	Number of samples
n, m, q	=	index
p	=	pressure
$\mathcal{P}$	=	polynomial function
P	=	induced velocity point of interest
ρ	=	density
$\mathcal{R}$	=	polynomial residual function
R	=	distance to vortex core
t	=	wing thickness function
T	=	temperature
θ	=	lifting line geometric angle

*Research Aerospace Engineer, Aeroacoustics Branch, MS 461, AIAA Senior Member
†Research Aerospace Engineer, Computational AeroSciences Branch, MS 128, AIAA Member
‡Senior Research Engineer, Aeroacoustics Branch, MS 461, AIAA Associate Fellow

V = velocity
x = axial coordinate
y = lateral coordinate
z = vertical coordinate

Subscripts
b = side of body
Γ = circulation
∞ = freestream
$L = 0$ = zero lift
max = maximum value in training data
min = minimum value in training data
w = wing
s = strut

Superscripts
$\hat{}$ = normalized
$\tilde{}$ = estimate

I. Introduction

Landing gear are typically a prominent source of noise at low-power flight conditions. As such, the accuracy of landing gear prediction methods is critical for the accuracy of the overall aircraft system noise prediction. Approaches to estimate landing gear noise generally fall into the categories of semiempirical methods [1–3] or computational methods, which rely on the local flow field and unsteady surface pressure to estimate the far field acoustic levels via the Ffowcs Williams and Hawkings equation [4–8].

NASA has continuously supported activities to improve predictions and reduce the community impacts of subsonic transport aircraft noise. This often includes prediction of conceptual aircraft, which lack the details required to use a computational approach. For this reason (along with overall process time), semiempirical methods are preferred. However, semiempirical approaches are limited to configurations with underlying physics similar to the data that are used to calibrate the model coefficients.

One concept that has received considerable attention and funding by NASA is the transonic truss-braced wing (TTBW) [9]. This vehicle configuration utilizes an increased wing aspect ratio to reduce the induced drag in an effort to achieve a lower fuel burn. This aspect ratio increase is structurally enabled by a truss structure composed of main and jury (secondary) struts. The landing gear is integrated to fit within the fairing joining the fuselage and the main strut. When the main gear is deployed, it is located directly under the portion of the main strut with minimal dihedral. This portion of the strut has non-zero spanload [10], albeit much lower than the loading on the wing. The effect of the sectional lift coefficient on the main gear local flow velocity has been well-documented [2, 11, 12], with the circulation of the wing and high-lift system acting to reduce the local flow velocity, along with the radiated noise. Guo et al. [13] also showed that on a hybrid wing body configuration, the reduction of this circulatory effect mitigated the reduced flight speed of the hybrid wing body relative to a conventional aircraft. Returning to the current configuration, the velocity induced by the main wing loading on the TTBW main gear is tempered by the increased distance between the wing and gear (relative to the strut), but not so far that the main wing loading can be neglected entirely. Harrison et al. [10] also proposed an alternate high-lift system that included an inboard strut flap installed in the vicinity of the landing gear that also has the potential to alter the sectional lift coefficient. The confluence of these potential flow effects leads to uncertainty in using existing semiempirical models that are calibrated to simpler situations on conventional aircraft.

This paper seeks to reduce the uncertainty in estimates of the TTBW local flow velocity by following the approach utilized in Guo [11], Guo et al. [13] to develop a correlation between the local flow and noise levels from Reynolds-averaged Navier-Stokes (RANS) simulations. Section II discusses the computational approach and database underpinning this work. Section III highlights some general trends in the data to determine the dependent parameters that are used in the surrogate modeling. The model form of the polynomial surrogate and lifting line approaches to modeling the local flow velocity are provided in Section IV. Then, the process for training the models is detailed in Section V. Section VI

compares the quality of the candidate models for both the training and validation data. The application of this model to a full vehicle noise prediction, and the impact of the updated local flow velocity on the landing gear element noise is carried out in Section VII. Finally, Section VIII then summarizes the relevant conclusions of this modeling effort.

II. Computational Database

The computational database is developed from steady RANS simulations carried out in FUN3D [14] using the Spalart-Allmaras turbulence model[15]. The simulated TTBW geometry is based on the model used in the NASA Langley Research Center 14- by 22-Foot Subsonic Tunnel [10], increased in size to be representative of the full-scale vehicle. The full-scale, single-aisle vehicle is described in Harrison et al. [16], with a design mission to carry 154 passengers over a range of 3500 NM, at a nominal cruise Mach number of 0.8.

Three different configurations are simulated, all of which have the variable-camber Krueger leading edge extended and the landing gear stowed. The freestream properties used for all simulations are presented in Table 1, while Table 2 lists the different configurations that were gridded.

Table 1 The list of freestream properties for all configurations.

p_∞ [kPa]	T_∞ [K]	ρ_∞ [kg m^{-3}]	μ_∞ [kg m^{-1} s^{-1}]	c_∞ [m s^{-1}]
101.33	288.17	1.2249	1.7894×10^{-5}	340.30

Table 2 The list of RANS geometry configurations.

ID	Name	Flap Angle [°]	Strut Flap Angle [°]
1	Approach	30	0
2	Takeoff	10	0
3	Strut Flap	30	20

Prior to presenting further details of the simulation setup, some discussion is offered to justify the choice to perform these simulations with the landing gear stowed. The local flow velocity correlation developed here is intended to be used in conjunction with the broader landing gear noise prediction method described in Guo et al. [13]. That method relies on several sets of wind tunnel data to set empirical coefficients. The local flow velocity for those wind tunnel tests is defined as the empty test section flow at the location of the gear, consistent with the approach taken in the simulations here. The reduction in the local incoming flow when the gear are present is implicitly taken into account in the empirical parameters of the noise prediction model. This approach is restrictive only in the sense that the individual gear components (e.g., strut, wheels) should experience the same fractional reduction in local Mach number for both the application and underlying wind tunnel data from inserting the gear. The benefits of this approach for RANS simulations are reductions in cost, grid generation complexity, and convergence challenges in the wake of the gear. It also avoids the ambiguity that comes with determining the proper streamwise station for incoming flow velocity in simulations where the gear is deployed. The first is an approach configuration, with flaps deployed at 30° and the variable-camber Krueger leading edge extended, pictured in Fig. 1. Grids for all simulations are generated in HeldenMesh*.

Configuration 1 has a 280 million node unstructured grid. It is a mixed-element grid composed primarily of tetrahedral and prismatic cells with a smaller proportion of pyramidal cells. Numerical convergence for the simulations is judged based on the residual, coefficient of lift and coefficient of drag convergence. Additionally, initial simulations of the vehicle were compared to experimental data on lift and drag coefficients. PowerFLOW data from previously published work on this configuration by Ferris and Khorrami [4] is used as cross-code verification of the computational fluid dynamics (CFD) simulations. Three sites along the strut of the vehicle and seven sites along the wing of the vehicle at Mach 0.2 and an angle of attack of 6.1 degrees are examined. Generally good agreement is seen on the main element. Figure 2a shows the surface mesh over the wing near the fuselage of the vehicle for the configuration 1. The surface coefficient of pressure over the the wing near the fuselage is shown in Fig. 2b and exhibits no obvious grid-driven phenomenon.

*Specific vendor and manufacturer names are explicitly mentioned only to accurately describe the setup. The use of vendor and manufacturer names does not imply an endorsement by the U.S. Government, nor does it imply that the specified equipment is the best available.

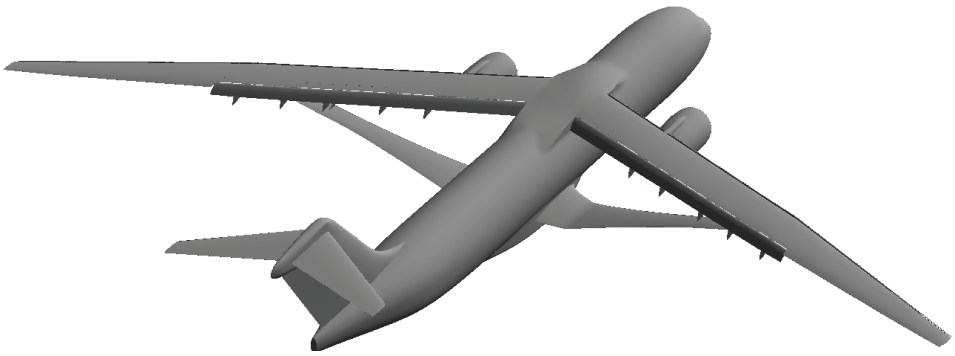

(a) Back isometric view of configuration 1

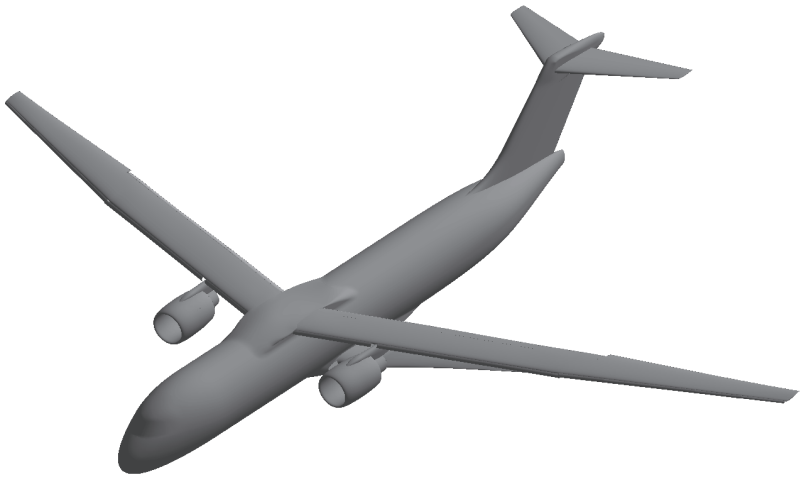

(b) Front isometric view of configuration 1

Fig. 1 Isometric views of the front and back of TTBW configuration 1.

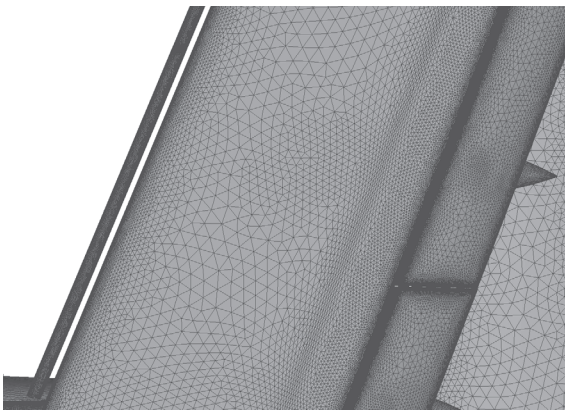

(a) Configuration 1 mesh over wing

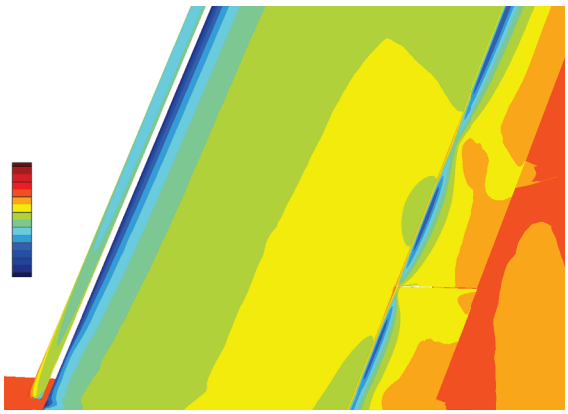

(b) Configuration 1 c_p over wing

Fig. 2 Configuration 1 wing mesh and pressure coefficient sample plots.

Table 3 lists the flight conditions that are simulated for this work. The approach configuration is listed as configuration 1. Simulations for this configuration are primarily comprised of an angle of attack sweep at a single flight speed, with the first four rows of Table 3 used as the model training data. Previous work [11], show that the local Mach number is

linearly related to the freestream flight Mach number. Further confirmation of this relation is obtained from unpublished RANS simulations of the TTBW with a cruise high-lift detent. Excellent collapse of the local velocity profile can be achieved by normalizing by the freestream Mach number. The flight speed and angles of attack are representative of the values from the flight path of the vehicle design used by June et al. [17] in an acoustic assessment of the TTBW. The remainder of the simulations for configuration 1, and the single case for configuration 2 serve as the validation set of the model, showing the model performance for Mach numbers, angle of attack, and detents (varying wing interaction) outside the scope of the training set.

Table 3 The list of simulated conditions for the three configurations.

Sim. ID	Config. ID	α [°]	M_∞
1	1	0.00	0.200
2	1	3.34	0.200
3	1	5.34	0.200
4	1	7.34	0.200
5	1	9.34	0.200
6	1	5.34	0.222
7	1	6.05	0.215
8	2	5.34	0.200
9	3	5.34	0.200

The second configuration is the takeoff configuration and changes the flap angle from 30° to 10°. This grid is a similar size to configuration 1, requiring about 280 million nodes. Figure 3a shows the surface mesh near the wing, and Fig. 3b shows the pressure coefficient over that same area. Table 3 shows the simulated test condition for configuration 2. This single simulation was completed with a Mach number matching the configuration 1 simulations, and an angle of attack of 5.34°, the median of the configuration 1 simulations. The configuration 2 simulation is used to evaluate the sensitivity of the local gear velocity field to the flap detent.

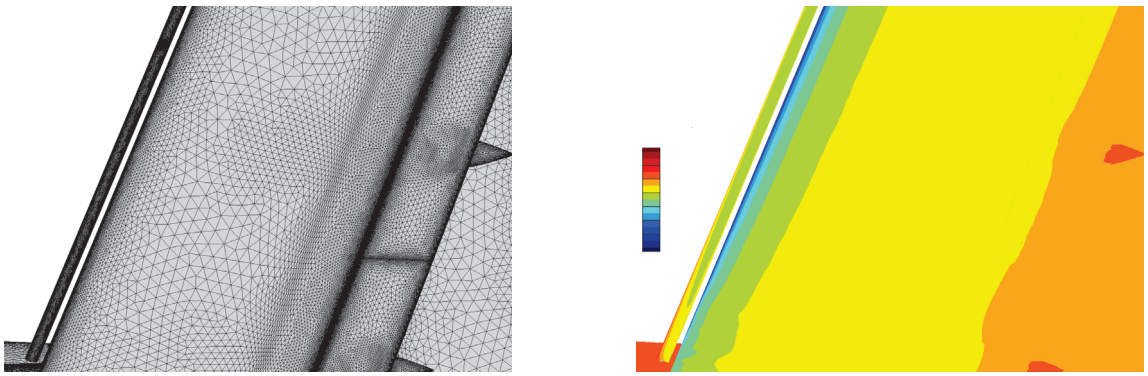

(a) Configuration 2 mesh over wing

(b) Configuration 2 c_p over wing

Fig. 3 Configuration 2 wing mesh and pressure coefficient sample plots.

The third and final configuration seen in Fig. 4 maintains the main wing flap angle of configuration 1 while adding a strut flap deployed at 20°. For this configuration, additional grid is required to resolve the strut flap, increasing the node count to 229 million. It is a mixed-element grid that is tetrahedral dominant, with a wing portion shown in Fig. 5a. A single simulation was run for the strut flap configuration at an angle of attack of 5.34° and at the same Reynolds number as the primary sweep for configuration 1. Comparing the coefficients of pressure for configurations 1 and 3 for the same spatial region shown in Fig. 2b, configuration 3 has significant differences on the wing surface in the area directly above the strut flap. The effect of the strut flap on the flow decreases in the spanwise direction and reaches a minimum at the wingtip.

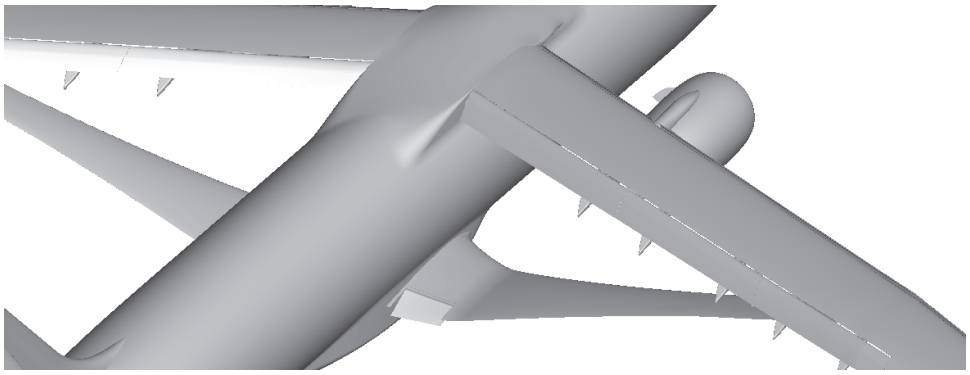

(a) Strut flap location

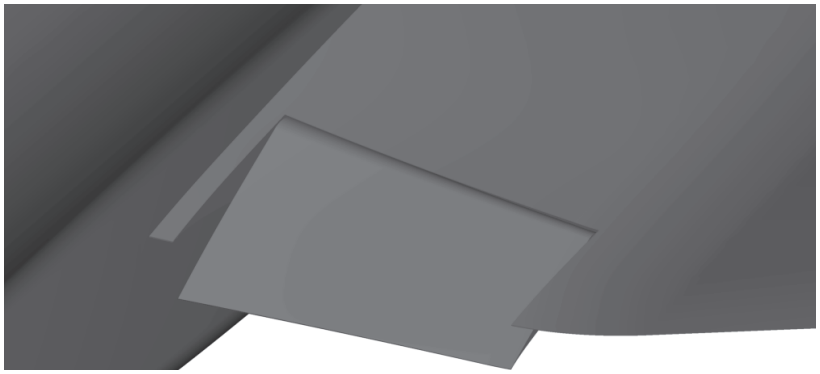

(b) Strut flap detail

Fig. 4 Configuration 3 showing the strut flap geometry.

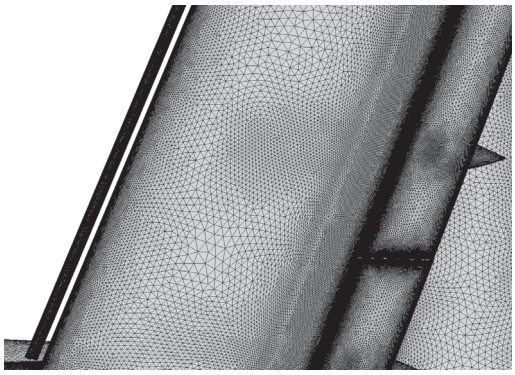

(a) Configuration 3 mesh over wing

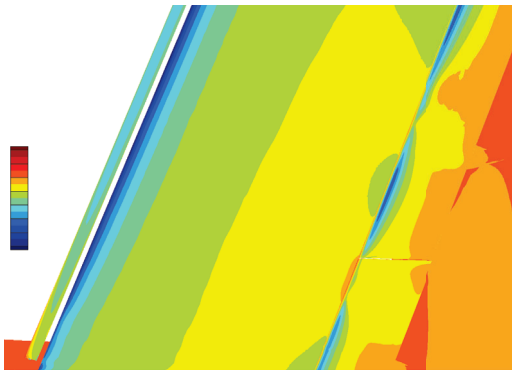

(b) Configuration 3 c_p over wing

Fig. 5 Configuration 3 wing mesh and pressure coefficient sample plots.

III. Main Gear Velocity Field Trends and Model Preparation

The velocity field is sampled in the region shown in Fig. 6 on the spanwise plane corresponding to the gear centerline. The coordinate axes follow the standard aircraft-centered definition: axial (longitudinal/roll axis), spanwise (lateral/pitch axis) and vertical (yaw axis). It is convenient for the modeling to normalize both the axial and vertical coordinates by the strut chord, (i.e., $\hat{x} = x/c$). The domain is bounded by $0.2 \leq \hat{x} \leq 0.8$ and $0 \leq \hat{z} \leq 3.75$, and is uniformly sampled with $\Delta\hat{x} = 0.01$ and $\Delta\hat{z} = 0.05$. The definition of $z = 0$ follows the outer mold line of the aircraft; at any x location, it describes the vertical distance to the strut surface. Stated differently, $z' = z + \frac{t(x)}{2}$, where z' is the vertical axis fixed to mean camber line, and t is the thickness of the airfoil. A simple Kriging model [18] is used to estimate the vertical

coordinate of the lower strut surface at the required points with a root mean square error (RMSE) on the order of $\hat{z} \approx 10^{-4}$.

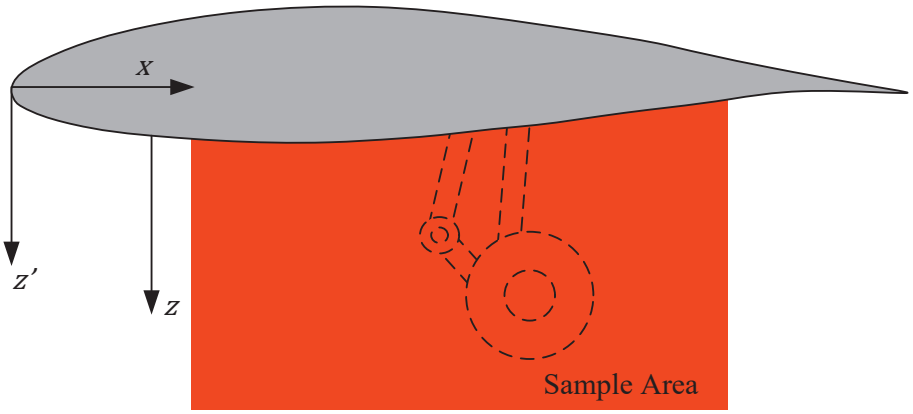

Fig. 6 A cartoon of representative (not to scale) geometry showing the integration of the gear into the strut is shown along with the velocity sampling domain. The approximate location of a hypothetical gear (also not to scale) is also shown.

Another advantage to simulating the vehicle with the landing gear stowed is that the model can easily account for variations in the streamwise position of the gear with a single simulation. This flexibility is used to determine whether the streamwise placement of the gear can be modified to reduce the radiated noise. Figure 7 shows the velocity field along the centerline (span) plane of the gear normalized by the velocity field at a hypothetical placement of a landing gear attachment at midchord, i.e., $\hat{M}(\hat{x},\hat{z})/\hat{M}(0.5,\hat{z})$. The outline of a gear strut and wheel is only for visualization, and

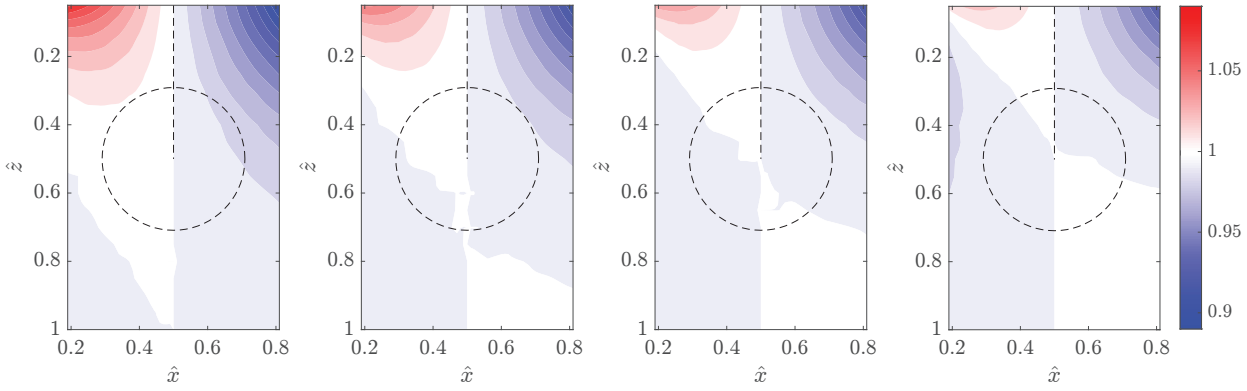

(a) $\alpha = 0°$ **(b)** $\alpha = 3.34°$ **(c)** $\alpha = 5.34°$ **(d)** $\alpha = 7.34°$

Fig. 7 The Mach fraction relative to the profile at $\hat{x} = 0.5$ is shown for the training data angles of attack with a representative gear outline.

does not correspond to the TTBW landing gear dimension. Local variations on the order of 10 % are present, which with a M^6 dependence could lead to source level variations on the order of 2.5 dB. While there is a potential noise benefit from moving the gear aft on the airfoil, the relative velocity reduction is less prominent at approach angles of attack. Noting that the color gradations correspond to one percent changes in the velocity, shifting the gear aft is unlikely to produce a noise reduction benefit sufficient to influence a system design trade over structural or other considerations. Optimization of the gear location for noise reduction is not pursued further.

Consideration is also given to including the effects of spanwise variation in the velocity field. The velocity field is sampled at several spanwise planes over the width of the gear bogie and compared to the velocity field at the landing

gear centerline. The RMSE of using the centerline velocity in the place of all the other planes is on the order of 0.25 % of the freestream velocity. This is considered sufficiently small to justify sampling the gear centerline plane alone for model development.

IV. Local Flow Model Form

As mentioned in Section I, the starting point for modeling is the model of Guo [11], which has proved reliable as part of the wider landing gear prediction scheme used on conventional tube and wing aircraft [19]. The model form is

$$\hat{M}(\alpha, \hat{z}) = \sum_{n=0}^{4} A_n \hat{z}^n - B(\alpha - 6), \tag{1}$$

where $\hat{M} = M/M_\infty$ and α is specified in degrees. However, initial comparisons with this model indicated that some interaction term between $\hat{z}$ and α is present, and can also be seen in the results of Guo [11]. Between this observation and the variations in the axial direction seen in Fig. 7, a more general modeling approach is used here. Models are drawn from the family of polynomials,

$$\hat{M}(\alpha, \hat{x}, \hat{z}) = \mathcal{P}(\alpha, \hat{x}, \hat{z}) = \sum_{q=0}^{2} \sum_{m=0}^{4} \sum_{n=0}^{4} A_{qmn} \alpha^q \hat{x}^m \hat{z}^n. \tag{2}$$

The final models that are used are very sparse relative to the number of possible terms to reduce the likelihood of overfitting. The process used to determine which terms are retained is discussed in Section V.

A second approach to modeling the local gear velocity builds on a previous application by Pott-Pollenske et al. [12] of lifting line theory to estimate the effect of the wing circulation. That work assumed a two-dimensional, constant circulation vortex filament. For the model here, we account for some three-dimensionality, treating the wing-body and strut-body junctions as termination points of the vortex filaments representing the wing and strut circulation, respectively. Figure 8 illustrates the geometry related to calculation of the wing circulation at the point P via the Biot-Savort law.

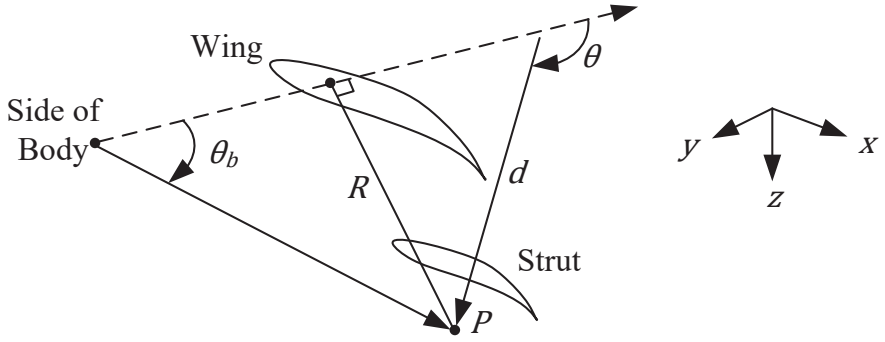

Fig. 8 An illustration of the lifting line geometry for a vortex centered at wing quarter chord. Adapted from Anderson [20].

For a semi-infinite vortex filament, the induced velocity at a point P is

$$V_\Gamma = -\frac{\Gamma}{4\pi R} \int_{\pi}^{\theta_b} \sin(\theta) d\theta = \frac{(1 + \cos\theta_b)\,\Gamma}{4\pi R} = \frac{k(R)\Gamma}{4\pi R}, \tag{3}$$

where $k(R)$ is a function of the aircraft geometry and location of P. R corresponds to the distance between P and the wing quarter-chord location. The vortex core path does not follow the true wing quarter-chord line in the spanwise direction. For convenience, vortex filament follows a simplified model of the wing airfoil. The airfoil coplanar with the gear centerline is assumed to extend spanwise without any sweep, taper, or dihedral. Past models have placed the vortex core vertically above the landing gear location [12] or at the center of lift [2]. However, for the case here, the former cannot be used since the landing gear would be aft of the entire main wing. The latter provides less consistent trends than the quarter-chord location, particularly near the zero-lift angle of attack of the strut. The procedure for the wing

can be repeated to calculate the effect of the strut circulation on P as well. Utilizing the Kutta-Joukowski theorem and the definition of the sectional lift coefficient, we arrive at the equation for the induced velocity

$$\hat{M}_\Gamma = \frac{k(\hat{R})\frac{dc_l}{d\alpha}\left(\alpha - \alpha_{L=0}\right)}{8\pi\hat{R}}. \tag{4}$$

A linear c_l-α relationship is sufficient to capture the trend at relevant approach angles of attack. Sectional lift values calculated directly from FUN3D for the wing and strut airfoils are used to least-squares fit a line for use at untested angles of attack.

While the circulation can be accounted for using the vortex filament, it does not account for perhaps the most important physical influence on the local gear velocity – the presence of the strut itself. In the absence of a straightforward analytical model, a polynomial function is fit to the residual velocity component, so that

$$\hat{M}\left(\alpha, \hat{x}, \hat{z}\right) = 1 - \hat{M}_{\Gamma,w}\left(\alpha, \hat{R}_w\right) - \hat{M}_{\Gamma,s}\left(\alpha, \hat{R}_s\right) + \mathcal{R}(\alpha, \hat{x}, \hat{R}_s) \tag{5}$$

where

$$\hat{R}_w = \frac{c_s}{c_w}\sqrt{\left(\hat{x} - 0.25 + \delta\hat{x}_{s,w}\right)^2 + \left(\hat{z} + \delta\hat{z}_{s,w}\right)^2}, \tag{6a}$$

$$\hat{R}_s = \sqrt{(\hat{x} - 0.25)^2 + \hat{z}^2}, \tag{6b}$$

and

$$\mathcal{R} = \sum_{q=0}^{2}\sum_{m=0}^{4}\sum_{n=0}^{4} A_{qmn}\alpha^q\hat{x}^m\hat{R}_s^n. \tag{6c}$$

Additionally, $\delta\hat{x}_{s,w}$ and $\delta\hat{z}_{s,w}$ are the axial and vertical distances between the wing and strut quarter-chord locations, respectively. The simple addition of individual terms is valid under the small angle approximation for both α and the direction angle between R and the z-axis. The half-thickness of the airfoil has also been neglected from the calculation of $\hat{R}_w$ and $\hat{R}_s$ to minimize the model complexity and input requirements.

On its face, this appears to effectively duplicate the approach in Eq. 2. The intent is to remove the vortex core effects, thereby generalizing the residual function to be less sensitive to changes in the wing and strut lift coefficients. This is tested using the configuration 2 simulation at a lower takeoff detent. An additional issue is that the residual velocity may be challenging to model near the singularity at strut quarter-chord. The extent of this issue should be evident through comparison of the training data to the fitted model.

In any model, it is prudent to guard against extrapolation outside of the range of the training data. For the situation here, we know that as $\hat{z} \to \infty$, $\hat{M} \to 1$. Accordingly, if the model is trained on data with $0 \le \hat{z} \le \hat{z}_{\max}$, it can be extended with a $\hat{z}^{-1}$ dependence, akin to the $\hat{R}^{-1}$ strength of vortex induced velocity.

$$\mathcal{P} = \begin{cases} \mathcal{P}, & \hat{z} \le \hat{z}_{\max} \\ 1 + \frac{\hat{z}_{\max}}{\hat{z}}\left(\mathcal{P}\left(\alpha, \hat{x}, \hat{z}_{\max}\right) - 1\right), & \hat{z} > \hat{z}_{\max} \end{cases} \tag{7}$$

For the vortex based method, the residual is modified to quickly decay to zero with $\hat{R}$ larger than the limits of the training data, where the circulation terms can be relied on to completely capture the the deviation from the freestream velocity. The extrapolation behavior chosen for this purpose is

$$\mathcal{R} = \begin{cases} \mathcal{R}, & \hat{R}_s \le \hat{R}_{s,\max} \\ \left(\frac{\hat{R}_{s,\max}}{\hat{R}_s}\right)^4 \mathcal{R}\left(\alpha, \hat{x}, \hat{R}_{s,\max}\right), & \hat{R}_s > \hat{R}_{s,\max} \end{cases} \tag{8}$$

The choice of a fourth power dependence is based on the rather arbitrary condition that at $2\hat{R}_{\max}$ the residual be about five percent of the value at $\hat{R}_{\max}$.

For most landing gear designs, sampling the velocity field to $\hat{z}_{\max} = 1$ (or $\hat{R}_{\max} = 1$) should be sufficient to encompass all of the gear sources, but there may be some unique situations (e.g., supersonic transports) where other design considerations result in long oleo struts.

V. Model Training

As discussed previously, simulations 1–4 of Table 3 are the source of training data. Prior to discussing the fitting process for the polynomials, an additional simplification is made to the lifting line model regarding the treatment of $k(\hat{R})$ in Eq. 3. Training data in the region $0.3 \leq \hat{x} \leq 0.65$ and $\hat{R} > 1$ is used to determine whether a constant, least-squares fit value of k is sufficient to capture the perturbation to the freestream Mach number in lieu of the full radial dependence. Ideally, this constant would capture the average impacts of the assumed vortex filament path and strength variations to provide an improved fit to the velocity data. Figure 9 illustrates both the bounds for the possible constants as well as the empirically fit values for a single angle of attack. The solid lines correspond to the mean value over the fit range of $\hat{x}$, while the filled surrounding regions of the same color represent the range of the data across $\hat{x}$ for a given value of $\hat{R}_s$. The plot on the left corresponds to the case where the vortex filament extends to infinity in both directions ($k = 2$, $\theta_b = 0$), the middle plot is the situation where the vortex filament ends at the side of body and P are coplanar ($k = 1$, $\theta_b = 90°$), and the right-hand plot corresponds to the empirical, least-squares fit. The empirical values work well for all angles of attack, while the quality of the infinite and semi-infinite (coplanar with side of body) assumptions varies with α. While these values do bring some empiricism into the model, it appeared at the time that the values were related to the geometry. Both constants are within three percent of the values of the minimum sample point tested (i.e., $k_w \approx k(\hat{R}_{w,\min})$) and $k_s \approx k(\hat{R}_{s,\min})$), and performed well for all α in the training set. Section VI.A shows that this is coincidental, and that the constants vary considerably for configuration 2.

Figure 9 also illustrates a clear challenge in the residual curve fitting approach for the lifting line models. Near the surface, removal of the strut lifting line contribution results in a larger magnitude residual in the near-body region, potentially hampering the accurate modeling of the near-body behavior by shifting the focus of the residual model to canceling the artifacts of removing the strut circulation term. As a compromise, an additional modeling approach is also considered: only the wing circulation is removed, and the residual function accounts for the both the strut circulation and near-body effects.

The shape of the residual data in Fig. 9 also seems to suggest that an exponential basis function may be more appropriate for $\mathcal{R}$ than the linear model chosen, also noting that an exponential would have the appropriate decay to zero far from the strut surface. Nonetheless, testing of alternate exponential basis function models did not result in substantial improvements to the fit quality, and the results are not reported here, for brevity.

With that simplification, the next step is to least-squares fit the polynomial families proposed in (Eqs. 2 and 6c. These have a large number of possible terms, and fitting to the entire set of coefficients is likely to overfit the dependence and lead to poor generalization. To combat this, an initial model including all the possible terms is fit. The RMSE between the training data $\hat{M}$ and the model prediction $\tilde{\hat{M}}$,

$$RMSE = \sqrt{\frac{1}{N}\left(\tilde{\hat{M}} - \hat{M}\right)^2}, \tag{9}$$

is then calculated. Hypothesis testing for the significance of each model coefficient [21] is utilized to recursively remove the least significant term until no terms remain. The test statistic used is the regression coefficient A_{lmn} divided by the standard error, as calculated by `fitlm`[22] in MATLAB2024a. Least significant is defined as the coefficient with the lowest absolute value of the test statistic. At each stage, the new RMSE is tabulated, and a stopping point is established where the RMSE begins to increase precipitously, as seen in Fig. 10. The RMSE at the stopping point for each of the models varies between 0.004–0.009. The training data used for fitting the various models is a subset of the domain mentioned in Section III, $0.3 \leq \hat{x} \leq 0.65$. This limits the impact of the larger deviations present at low and high chord fractions, and also limits the impacts of the region where the lifting line model is most impacted by the proximity to the assumed vortex core location. To justify this restriction, it is likely that this region is sufficient to capture the most likely gear installation locations. Additionally, the models are compared over the fuller region, $0.2 \leq \hat{x} \leq 0.8$ in comparisons prior to final validation to verify that this restriction doesn't greatly affect the quality of the fit. For the polynomial model, the training data is restricted to $0 \leq \hat{z} \leq 1$, while for the lifting line polynomials, it is $0 \leq \hat{R}_s \leq 1$. For the polynomial model, $\hat{z}$ is used instead of $\hat{R}_s$ because the two provide similarly sparse models for a particular RMSE threshold, and $\hat{z}$ is a simpler parameter to calculate. For the lifting line polynomial, $\hat{R}_s$ is retained as a dependent variable for consistency with the other model terms. It should also be noted that $\hat{R}_s$ provided marginally improved collapse of the velocity profile over $\hat{z}$ for the range of $\hat{x}$ used in training.

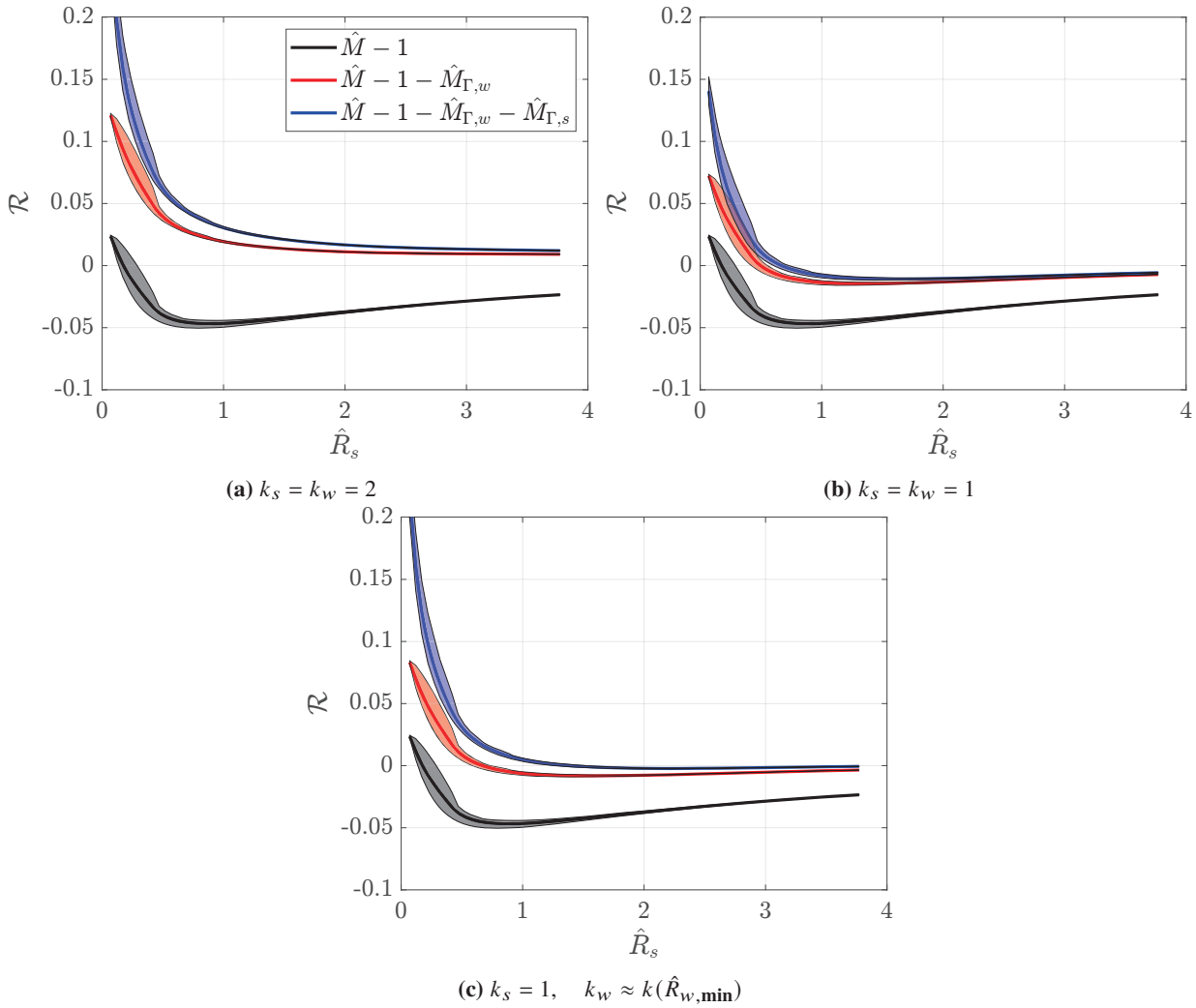

(a) $k_s = k_w = 2$

(b) $k_s = k_w = 1$

(c) $k_s = 1, \quad k_w \approx k(\hat{R}_{w,\mathbf{min}})$

Fig. 9 The plots show the average normalized Mach number deviation from freestream with and without the wing and or strut circulation terms for a single training case. Each plot has different assumptions regarding the vortex constant k, corresponding to (a) infinite, (b) semi-infinite coplanar to side of body, and (c) semi-infinite with empirically fit values.

VI. Model Results

With the completion of model training, this section provides the resulting performance of the models on the training set, followed by discussion and comparison of the models for the validation cases. Several variants to the models with different assumptions or forms are considered throughout and are also discussed throughout this section. However, the majority of the data presented focuses on four models. Two are polynomial models, one with dependence on $\hat{x}$ and one without. The model without $\hat{x}$ dependence is retained as it could possibly generalize to the validation data at the cost of increased RMSE for the training set. The sparse set of model coefficients for these models are

$$\mathcal{P}\left(\alpha, \hat{z}\right) = A_{000} + A_{100}\alpha + A_{101}\alpha\hat{z} + A_{001}\hat{z} + A_{002}\hat{z}^2 \tag{10a}$$

and

$$\mathcal{P}\left(\alpha, \hat{x}, \hat{z}\right) = A_{000} + A_{100}\alpha + A_{101}\alpha\hat{z} + A_{001}\hat{z} + A_{002}\hat{z}^2 + A_{012}\hat{x}\hat{z}^2 + A_{110}\alpha\hat{x} + A_{020}\hat{x}^2 + A_{021}\hat{x}^2\hat{z} \tag{10b}$$

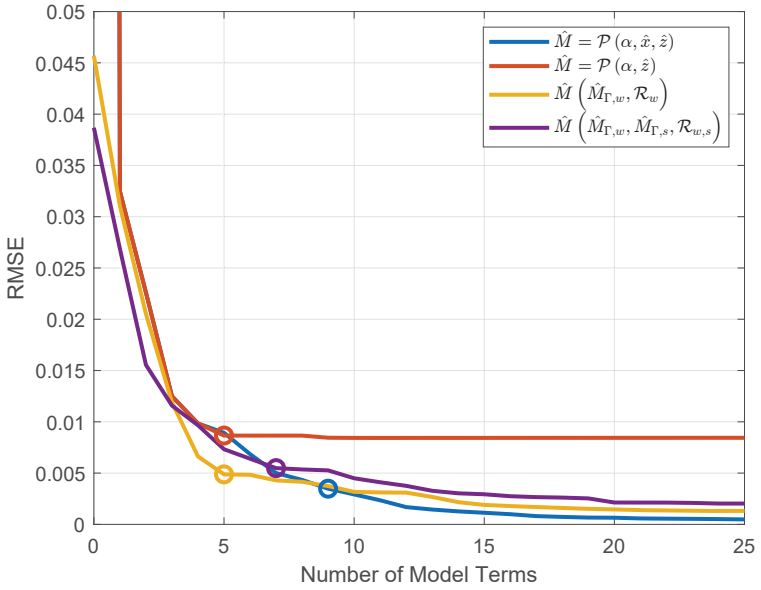

Fig. 10 The plots show the RMSE as a function of the number of terms retained in the model. The circled locations correspond to the chosen model form.

The other two are the lifting line models, one that includes a circulation term for the strut, and one that does not. The residual functions are

$$\mathcal{R}_w\left(\alpha, \hat{x}, \hat{R}_s\right) = A_{000} + A_{100}\alpha + A_{101}\alpha\hat{R}_s + A_{001}\hat{R}_s + A_{002}\hat{R}_s^2 \tag{11a}$$

and

$$\mathcal{R}_{w,s}\left(\alpha, \hat{x}, \hat{R}_s\right) = A_{001}\hat{R}_s + A_{002}\hat{R}_s^2 + A_{003}\hat{R}_s^3 + A_{100}\alpha + A_{101}\alpha\hat{R}_s + A_{102}\alpha\hat{R}_s^2 + A_{103}\alpha\hat{R}_s^3 \tag{11b}$$

for the case with the wing lifting line term alone, and the model including lifting line terms for both wing and strut, respectively. Note the absence of an $\hat{x}$ dependence in both residual functions (apart from the implicit dependence in $\hat{R}_s$). While it is encouraging that the $\hat{R}_s$ appears to be the correct parameterization for this function, recall that Fig. 9 showed that subtracting the strut circulation from the data increased the magnitude of the residual, so that the main trend captured by the residual function is to counter that $\hat{R}_s^{-1}$ dependent effect rather than the near-body flow dependence.

The mean absolute error of these models compared to the training cases is shown in Fig. 11. The error in the region used to train the data is fairly devoid of features. Outside of that range, there are several features worth discussing.

For the polynomial models in the region $\hat{z} > 1$, the error is much larger than that of the lifting line models. The extrapolation procedure discussed in Eq. 7 reduces the RMSE in the region $\hat{z} > 1, 0.3 \leq \hat{x} \leq 0.65$ from 0.485 to 0.0127. One may also be tempted to fit a polynomial to the full range of $\hat{z}$, which would further reduce the RMSE in this domain to 0.0027. However, doing so ends up sacrificing performance near the wall, increasing the RMSE from 0.0037 ($\hat{z} < 1$) to 0.0095 (all $\hat{z}$).

The value of introducing an $\hat{x}$ dependence in the polynomial model is seen in the region near the strut surface. The $\mathcal{P}(\alpha, \hat{x}, \hat{z})$ function is able to more accurately reproduce the velocity field near the quarter-chord and aft section near the wall. For the lifting line models, the quality of the fit is good everywhere with the exception of the upstream, near-wall region. The model that includes the strut circulation term has a particularly inaccurate region local to the quarter-chord as $\hat{R}_s \to 0$.

Table 4 presents the RMSE values of each model for the combination of all the training data simulation conditions broken into three regions of the data. Zone A corresponds to $0.3 \leq \hat{x} \leq 0.65$, $\hat{z} < 1$ while Zone B is $0.2 \leq \hat{x} \leq 0.8$ and $\hat{z} < 1$. Zone C is the full data set, $0.2 \leq \hat{x} \leq 0.8$ and $0 \leq \hat{z} \leq 3.75$.

While the inclusion of $\hat{x}$ in the polynomial appears to improve the quality of the fit across some training and validation data, the improvement does not consistently generalize to have a significant advantage in including the dependence in the model.

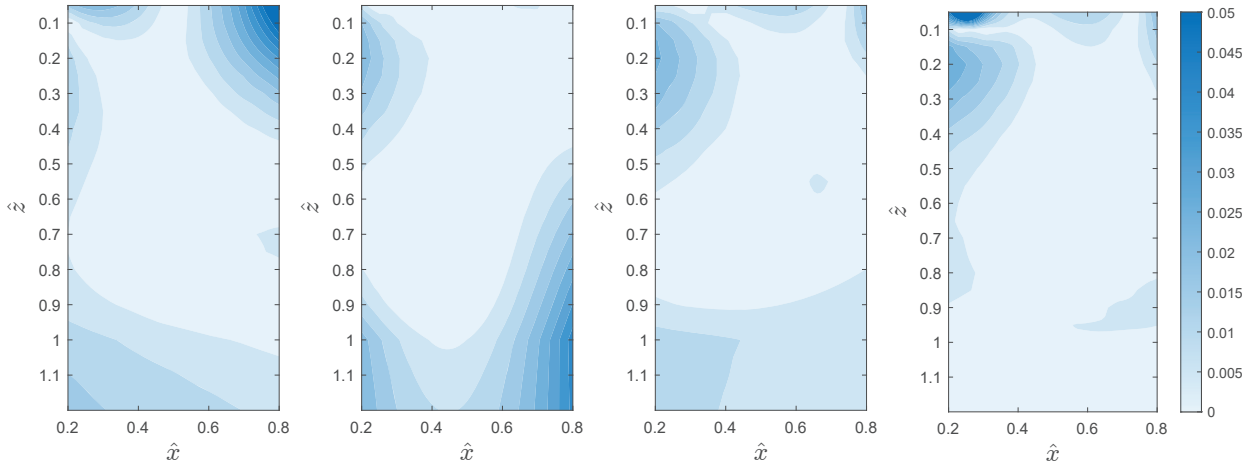

(a) $\hat{M} = \mathcal{P}(\alpha, \hat{z})$ **(b)** $\hat{M} = \mathcal{P}(\alpha, \hat{x}, \hat{z})$ **(c)** $\hat{M}\left(\hat{M}_{\Gamma,w}, \mathcal{R}_w\right)$ **(d)** $\hat{M}\left(\hat{M}_{\Gamma,w}, \hat{M}_{\Gamma,s}, \mathcal{R}_{w,s}\right)$

Fig. 11 The absolute error between each model and the training data at angle of attack of 7.34°. The limits on the plot have a fixed value of 0.05 to allow for a better comparison over the full domain. This maximum value is exceeded locally in (a) near the strut trailing edge and (d) near the quarter-chord location.

Table 4 The RMSE of each model for the training data for different data ranges.

Model	Zone A ($\times 10^{-3}$)	Zone B ($\times 10^{-3}$)	Zone C ($\times 10^{-3}$)
$\hat{M} = \mathcal{P}\left(\alpha, \hat{x}, \hat{z}\right)$	3.7	7.8	14.5
$\hat{M} = \mathcal{P}\left(\alpha, \hat{z}\right)$	8.5	15.4	13.4
$\hat{M}\left(\hat{M}_{\Gamma,w}, \mathcal{R}_w\right)$	5.0	6.7	5.6
$\hat{M}\left(\hat{M}_{\Gamma,w}, \hat{M}_{\Gamma,s}, \mathcal{R}_{w,s}\right)$	5.4	10.4	5.4

The performance of the models is consistent with the training data for simulations 6 and 7, illustrating the insensitivity to M_∞ and the ability to estimate the velocity trends for α within the limits of the training data. For simulation 5, the RMSE is slightly increased in both zones and for all models, except $\mathcal{P}(\alpha, \hat{z})$ which shows nearly equivalent RMSE as $\mathcal{P}(\alpha, \hat{x}, \hat{z})$ and improved performance relative to the training set.

A. Wing Detent Influence

It has been shown that the main wing exerts influence over the velocity field near the gear. However, what is less clear is if the difference in the main wing lift at various detents is sufficient to warrant additional modeling. This question is addressed through the results of simulation 8, where configuration 2 has been simulated and estimated with the models trained on configuration 1 data. The performance of the $\mathcal{P}(\alpha, \hat{z})$ model (see Table 5) is in line with the other validation cases, indicating that this model is relatively insensitive to the change in the velocity field due to the change in detent.

However, the lifting line models do not perform well for this validation case. In fact, the RMSE improves if you used the c_l-α relationship for the approach detent rather than directly using the sectional lift calculated by FUN3D for the takeoff detent. In Zone A, the RMSE is reduced to 0.0083 and 0.0085 for the wing lifting line and combined wing-strut lifting line models, respectively. Zone B shows similar improvements. This indicates that removal of the circulation terms is not generalizing well. The larger reduction in RMSE for the combined wing-strut lifting line model also shows that the velocity field is (as might be expected) much more sensitive to the strut circulation term for $\hat{z} < 1$.

Due to the issue being found in the validation procedure, there was limited time prior to publication to attempt to improve the lifting line models. However, based on the absolute differences in $\hat{M}$ between the approach (simulation 3) and takeoff detent (simulation 8) shown in Fig. 12, there is minimal difference in the region of interest, indicating the polynomial models should still perform well. Specifically, the RMSE between the CFD solution for both cases is 0.0069, 0.0078, and 0.0086 for Zones A, B, and C, respectively. This is on the order of the difference of the models to

Table 5 The RMSE of each validation case for Zones A and B.

Model	Simulation 5		Simulation 6		Simulation 7		Simulation 8	
	Zone A ($\times 10^{-3}$)	Zone B ($\times 10^{-3}$)	Zone A ($\times 10^{-3}$)	Zone B ($\times 10^{-3}$)	Zone A ($\times 10^{-3}$)	Zone B ($\times 10^{-3}$)	Zone A ($\times 10^{-3}$)	Zone B ($\times 10^{-3}$)
$\hat{M} = \mathcal{P}(\alpha, \hat{x}, \hat{z})$	5.0	10.4	3.4	7.8	3.3	7.5	7.5	8.5
$\hat{M} = \mathcal{P}(\alpha, \hat{z})$	4.8	9.1	6.3	11.7	6.9	12.7	8.0	11.4
$\hat{M}\left(\hat{M}_{\Gamma,w}, \mathcal{R}_w\right)$	6.9	8.9	5.1	6.3	4.9	6.0	14.7	16.7
$\hat{M}\left(\hat{M}_{\Gamma,w}, \hat{M}_{\Gamma,s}, \mathcal{R}_{w,s}\right)$	8.3	15.9	4.6	6.9	4.1	5.7	43.5	50.8

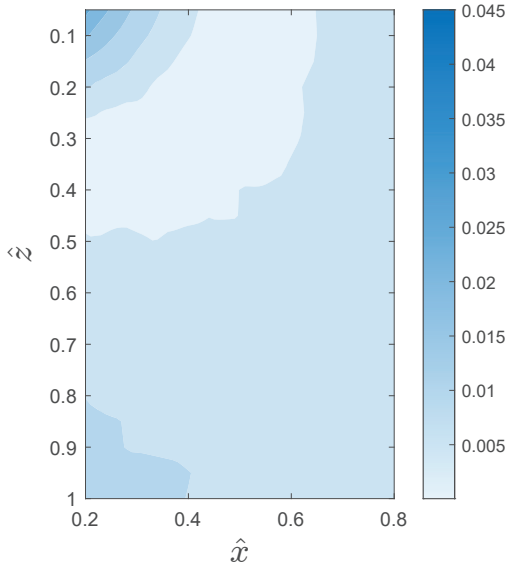

Fig. 12 The absolute difference between the takeoff and approach detent normalized Mach number field at an angle of attack of 5.34°.

the training data, indicating that not much accuracy is lost on the models that do not use the sectional lift coefficient as an input.

While the RMSE indicates that globally there is not much difference between the velocity fields of the approach and takeoff detent cases, there are some large local deviations. A radial error pattern is present near the leading edge, and if the gear are place here, it is possible that some of the landing gear sources near the strut could have local Mach number differences important enough to impact the noise prediction of the gear. The uncertainties in properly modeling (if possible) the effects of the lifting line contribution lead to a preference in predicting the TTBW gear velocity using one of the polynomial models.

B. Strut Flap Local Velocity Effects

The strut flap case is intended as an additional validation case to both understand the noise reduction potential of the device and perturb the sectional lift of the strut independent of the main wing detent. After the failure of the lifting line model to generalize to other sectional lift values, the main purpose of this section is to determine whether the strut flap is a viable noise reduction path.

To do so, the local velocity fields are compared between the cases with and without the strut flap deflected, shown in Fig. 13. The difference is typically within 2–3 % for locations where a majority of the gear sources would be present. These differences are not strongly dependent on angle of attack. Assuming a sixth-power relationship with Mach number, the strut flap deflection produces a source level noise reduction of 0.5–0.8 dB SPL. While this at first may seem worthwhile to pursue, particularly if the main landing gear is a dominant source, there are also downsides for noise generation that mitigate the usefulness of the strut flap. For instance, the strut flap introduces additional flap side

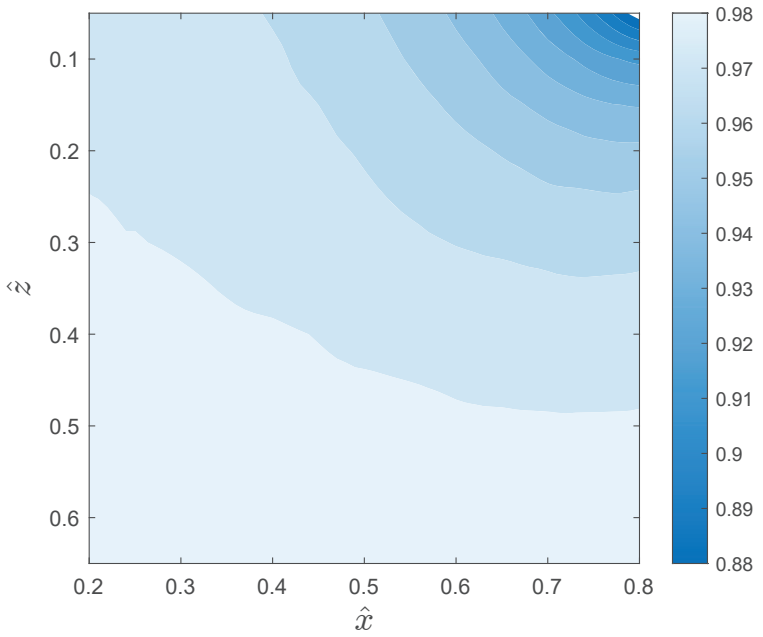

Fig. 13 The Mach number fraction of the case with that strut flap deployed relative to the stowed case on the plane of the main landing gear strut centerline for an angle of attack of 5.34°.

edge noise sources and a potential interaction noise source between the gear wake and the flap. For these reasons, no additional simulation or modeling of the strut flap effect is included here. It is possible that an alternative implementation of the strut flap to achieve a greater effect on reducing main gear noise, perhaps by adding Fowler motion to the flap. Another approach could be to modify the strut airfoil geometry to locally increase the sectional lift coefficient. As final clarification, the strut flap clearly impacts the velocity field, and if it is included in the final vehicle design, the effects should be incorporated into the local Mach model.

VII. Impact on Noise Prediction

A simulation of the TTBW gear in an approach flight condition is valuable for understanding the quantitative impacts of developing a model that is specific to the TTBW. This section addresses the tools and setup for assessing the baseline TTBW aircraft from previous work [17]. It also covers the impact of the modeling at the component (e.g., main gear) level.

A. ANOPP Model

Simulation of the baseline TTBW is discussed in depth elsewhere [17], and only the relevant details are reproduced here. The vehicle is a single-aisle transport with a design range of 3500 NM carrying 154 passengers. The engine is a direct drive cycle [16] modeled using the Numerical Propulsion Simulation System [23]. While sharing significant heritage with the Boeing design, the vehicle simulated here is resized using the FLight OPtimization System (FLOPS) [24]. FLOPS also provides a takeoff and landing profile that is compliant with noise certification regulations in Title 14 Part 36 of the Code of Federal Regulations [25].

For the noise prediction, the Aircraft NOise Prediction Program (ANOPP) is used for source level generation and modification for noise reduction technologies and the propulsion airframe aeroacoustic effects. ANOPP is run from within the ANOPP2 framework [26], which propagates the source noise levels to the ground observer via the ANOPP2 Straight Ray Propagation Internal Functional Module (ASRPIFM). ANOPP2 also provides post-processing capabilities to calculate the effective perceived noise level (EPNL). The results discussed here are taken at the component level, where the landing gear is predicted using the approach of Guo et al. [13].

B. Main Gear Noise Results

The approach certification point is used to show the impacts of the local velocity modeling on the landing gear noise. The TTBW approach conditions compliant with noise certification are $\alpha = 5.34°$ to maintain a 3° glide slope, flight Mach number of 0.19, and the high-lift system deployed at the flaps 30 detent.

Several different variations of the local flow velocity treatment are compared. The first model uses an existing landing gear correlation in ANOPP for conventional tube-and-wing body gear. The second model assumes that the local inflow velocity is equivalent to the freestream. The third model is the polynomial model from Section VI, $\hat{M} = \mathcal{P}(\alpha, \hat{z})$, and the final model interrogates the RANS simulation directly to determine the local velocity.

Prior predictions of the TTBW assumed that the landing gear could be modeled similarly to the body gear of a conventional tube and wing aircraft (e.g., A340 centerline main gear). The rational for this assumption is that the local flow velocity for the TTBW strut-mounted gear is similar to what a body gear sees. However, the reflection of landing gear noise from a body gear is also significantly different from that of a wing or strut mounted gear. To isolate the local Mach number effects, the effects of gear reflection are excluded. The reflection effects calculated by ANOPP vary depending on the landing gear type and geometry.

Table 6 provides the EPNL for all velocity models considered for use in the system noise assessment. First, minimal

Table 6 Comparison of main gear EPNL for different local velocity models.

Model	Main Gear Level (EPNdB)
Body Gear	72.48
$\hat{M} = 1$	70.51
$\hat{M} = \mathcal{P}(\alpha, \hat{z})$	70.05
RANS	70.10

differences between direct use of the RANS solution in the prediction and the polynomial model verifies that the polynomial model is sufficient for system noise predictions. Second, it is clear that the polynomial model is much more consistent with the RANS solution over the previously-assumed body gear model, which has an error of 2.4 EPNdB. The polynomial model is within 0.1 EPNdB of the result of the RANS solution, while the freestream assumption is next best with a 0.4 EPNdB difference. In the absence of experimental noise measurements of the TTBW main gear, it is difficult to conclusively validate that agreement with the RANS solution corresponds with an improvement in the noise prediction. However, it is worth repeating that the RANS simulations are in line with fluid dynamic measurements taken in a wind tunnel entry [10], and that use of this prediction model framework has performed well in predicting conventional aircraft [19].

This paper has focused on the unique main gear installation for a TTBW. However, the RANS simulations also provided an additional data set with which to test the nose gear correlation presented in Guo [11]. A similar process to the training described in Section V is used to fit a correlation to the region of the TTBW geometry where the nose gear is installed. Prediction of the nose gear using both models showed agreement within 0.2 EPNdB.

VIII. Conclusions

This work reaffirmed the value of using RANS data to improve the assumed landing gear local Mach number relationship for unconventional configurations. Although several candidate models are developed, ultimately the simplest model is retained for TTBW predictions. This polynomial model has the same variable dependency as what was introduced by Guo [11], although the model form here is slightly different. The process to establish a model based on sequential removal of the least significant coefficient resulted in a sparse form desirable for system noise analysis while still retaining sufficient accuracy. Ultimately, the polynomial surrogate model trained on the TTBW CFD data improved agreement with the RANS profile relative to the method used in a previous assessment [17], removing the bias (relative to the RANS solution) of 2.4 EPNdB from the noise prediction.

Notably, this simple polynomial model performed better than the more physics-based lifting line models. The validation case at the takeoff high-lift detent illustrated that an empirical parameter fitted to the data where $\hat{z} > 1$ is not, in fact, geometry related. The exact dependence of this parameter, and even whether this is a valid modeling approach for this geometry remains unclear. Additionally, the inability to establish the empirical parameters based on the geometry alone means that the lifting line models required data at $\hat{z} > 1$ to be fit (see Section V). While it may be

possible to estimate those coefficients using data within the training set, that has not yet been attempted. On the other hand, the polynomial method has been modified to take a piecewise approach to separate interpolated and extrapolated values. Utilizing an extrapolation procedure that emulates the inverse distance relationship present in the lifting line theory, the polynomial model is able to replicate the well-behaved behavior of the lifting line models at large values of $\hat{z}$.

With only a single instance of a TTBW configuration, it is an open topic as to whether the polynomial model is general enough to accurately predict the local flow of other TTBW configurations with different geometry or wing-strut design philosophy. It is recommended that evaluation of panel methods relative to CFD be carried out in future work, as panel methods potentially provide the appropriate mix of qualities needed for system noise assessment; panel methods are able to reduce the setup complexity and cycle time relative to RANS, while generalizing better than the polynomial models.

Lastly, results indicate that the strut flap is unlikely to be successful at providing appreciable noise reduction for the TTBW landing gear. A simple hinge flap does not increase the lift enough to have a large decrease in the local flow velocity. Consideration of a flap with Fowler motion will provide additional gear velocity reduction, but could introduce other undesirable noise sources (e.g., gear-flap interaction noise). A design trade for including the strut flap would also need to consider the increased weight and complexity of adding Fowler motion. An alternate approach to gear noise reduction could be the podded landing gear proposed in Thomas et al. [27].

Acknowledgments

The Advanced Air Transport Technology Project is acknowledged for funding this work. The authors would like to thank Nik Zawodny, Jordan Kreitzman, Ian Clark, and Russell H. Thomas for technical review. David P. Lockard is gratefully acknowledged for his help in coordinating the development of the computational database. The Boeing Company is acknowledged for generation of the aircraft geometry. All simulations were performed on the K-Cluster computers at NASA Langley Research Center.

References

[1] Fink, M. R., "Airframe Noise Prediction Method," FAA-RD-77-29, 1977.

[2] Smith, M., Carrilho, J., Molin, N., Piet, J.-F., and Chow, L., "Modelling of Landing Gear Noise with Installation Effects," *AIAA Paper 2007–3472*, May 2007. doi:10.2514/6.2007-3472.

[3] Lopes, L. V., Brentner, K. S., and Morris, P. J., "Framework for a Landing-Gear Model and Acoustic Prediction," *Journal of Aircraft*, Vol. 47, No. 3, 2010, pp. 763–774. doi:10.2514/1.36925.

[4] Ferris, R., and Khorrami, M. R., "Aeroacoustic Computations of a Transonic Truss-Braced Wing Aircraft: Part 1 – Aerodynamic and Airframe Noise Simulations," *AIAA Paper 2024–3058*, June 2024. doi:10.2514/6.2024-3058.

[5] Ravetta, P. A., Khorrami, M. R., and Ferris, R., "Aeroacoustic Computations of a Transonic Truss-Braced Wing Aircraft: Part 2 – Acoustic Signature and Noise Source Identification," *AIAA Paper 2024-3059*, June 2024. doi:10.2514/6.2024-3059.

[6] Imamura, T., Hirai, T., Amemiya, K., Yokokawa, Y., Enomoto, S., and Yamamoto, K., "Aerodynamic and aeroacoustic simulations of a two-wheel landing gear," *Procedia Engineering*, Vol. 6, 2010, pp. 293–302. doi:https://doi.org/10.1016/j.proeng.2010.09.031.

[7] Lockard, D., Khorrami, M., and Li, F., "Aeroacoustic Analysis of a Simplified Landing Gear," *AIAA Paper 2003-3111*, May 2003. doi:10.2514/6.2003-3111.

[8] Casalino, D., Ribeiro, A. F. P., Fares, E., and Nölting, S., "Lattice–Boltzmann Aeroacoustic Analysis of the LAGOON Landing-Gear Configuration," *AIAA Journal*, Vol. 52, No. 6, 2014, pp. 1232–1248. doi:10.2514/1.J052365.

[9] Droney, C. K., Harrison, N. A., and Gatlin, G. M., *Subsonic Ultra-Green Aircraft Research: Transonic Truss-Braced Wing Technical Maturation*, September 2018. URL `http://www.icas.org/ICAS_ARCHIVE/ICAS2018/data/papers/ICAS2018_0597_paper.pdf`.

[10] Harrison, N. A., Gatlin, G. M., Viken, S. A., Beyar, M., Dickey, E. D., Hoffman, K., and Reichenbach, E. Y., "Development of an Efficient M=0.80 Transonic Truss-Braced Wing Aircraft," *AIAA Paper 2020–0011*, January 2020. doi:10.2514/6.2020-0011.

[11] Guo, Y., "Effects of Local Flow Variations on Landing Gear Noise Prediction and Analysis," *Journal of Aircraft*, Vol. 47, No. 2, 2010, pp. 383–391. doi:10.2514/1.43615.

[12] Pott-Pollenske, M., Dobrzynski, W., Buchholz, H., Guérin, S., Saueressig, G., and Finke, U., "Airframe Noise Characteristics from Flyover Measurements and Prediction," *AIAA Paper 2006–2567*, May 2006. doi:10.2514/6.2006-2567.

[13] Guo, Y., Burley, C. L., and Thomas, R. H., "Landing Gear Noise Prediction and Analysis for Tube-And-Wing and Hybrid-Wing-Body Aircraft," *AIAA Paper 2016–1273*, January 2016. doi:10.2514/6.2016-1273.

[14] Anderson, W. K., Biedron, R. T., Carlson, J.-R., Derlaga, J. M., Diskin, B., Druyor Jr., C. T., Gnoffo, P. A., Hammond, D. P., Jacobson, K. E., Jones, W. T., Kleb, B., Lee-Rausch, E. M., Liu, Y., Nastac, G. C., Nielsen, E. J., Padway, E. M., Park, M. A., Rumsey, C. L., Thomas, J. L., Thompson, K. B., Walden, A., Wang, L., Wood, S. L., Wood, W. A., and Zhang, X., "FUN3D Manual: 14.1," NASA/TM-20240006306, June 2024. URL https://ntrs.nasa.gov/citations/20240006306.

[15] Spalart, P. R., and Allmaras, S. R., "A One-Equation Turbulence Model for Aerodynamic Flows," *La Recherche Aérospatiale*, Vol. 1, No. 1, 1994, pp. 5–21. URL https://turbmodels.larc.nasa.gov/Papers/RechAerosp_1994_SpalartAllmaras.pdf.

[16] Harrison, N. A., Hoffman, K., Lazzara, D. S., Reichenbach, E. Y., Sclafani, A. J., and Droney, C. K., "Subsonic Ultra Green Aircraft Research: Phase IV Final Report – Volume I Mach 0.80 Transonic Truss-Braced Wing High-Speed Design Report," NASA/CR-20220016017/Vol. I, October 2023. URL https://ntrs.nasa.gov/citations/20220016017.

[17] June, J., Thomas, R. H., and Guo, Y., "System Noise Technology Roadmaps for a Transonic Truss-Braced Wing and Peer Conventional Configuration," *AIAA Paper 2022–3049*, June 2022. doi:10.2514/6.2022-3049.

[18] Fang, K.-T., Li, R., and Sudjianto, A., *Design and Modeling for Computer Experiments*, 1st ed., Chapman and Hall/CRC, 2006. doi:https://doi.org/10.1201/9781420034899.

[19] Guo, Y., and Thomas, R. H., "Assessment of Next Generation Airframe System Noise Prediction Methods with PAA and ASN Flight Test Data," *AIAA Paper 2022–2995*, June 2022. doi:10.2514/6.2022-2995.

[20] Anderson, J. D. J., *Fundamentals of Aerodynamics*, 4th ed., McGraw-Hill, 2007.

[21] Montgomery, D. C., *Design and analysis of experiments*, 10th ed., Wiley, 2020.

[22] The Mathworks, Inc., "fitlm," , 2025. URL https://www.mathworks.com/help/stats/fitlm.html.

[23] Lytle, J. K., "The Numerical Propulsion System Simulation: An Overview," NASA TM-2000-209915, June 2000. URL https://ntrs.nasa.gov/citations/20000063377.

[24] McCullers, L., "Aircraft Configuration Optimization Including Optimized Flight Profiles," *Proceedings of the Symposium of Recent Experiences in Multidisciplinary Analysis and Optimization*, NASA CP-2327, 1984, pp. 395–412. URL https://ntrs.nasa.gov/citations/19870002310.

[25] *Noise Standards: Aircraft Type and Airworthiness Certification*, Code of Federal Regulations, Title 14, Chapter 1, Part 36, January 2024.

[26] Lopes, L. V., and Burley, C. L., "ANOPP2 User's Manual, Version 1.2," NASA/TM-2016-219342, October 2016. URL https://ntrs.nasa.gov/citations/20160014858.

[27] Thomas, R. H., Nickol, C. L., Burley, C. L., and Guo, Y., "Potential for Landing Gear Noise Reduction on Advanced Aircraft Configurations," *AIAA Paper 2016–3039*, May 2016. doi:10.2514/6.2016-3039.